Nido-Hydroborate-Based Electrolytes for All-Solid-State Lithium Batteries

Payandeh, SeyedHosein ; Rentsch, Daniel ; Łodziana, Zbigniew ; Asakura, Ryo ; Bigler, Laurent ; Černý, Radovan ; Battaglia, Corsin ; Remhof, Arndt

Abstract: Hydroborate-based solid electrolytes have recently been successfully employed in high voltage, room temperature all-solid-state sodium batteries. The transfer to analogous lithium systems has failed up to now due to the lower conductivity of the corresponding lithium compounds and their high cost. Here LiB11H14 nido-hydroborate as a cost-effective building block and its high-purity synthesis is introduced. The crystal structures of anhydrous LiB11H14 as well as of LiB11H14-based mixed-anion solid electrolytes are solved and high ionic conductivities of 1.1 × 10−4 S cm−1 for Li2(B11H14)(CB11H12) and 1.1 × 10−3 S cm−1 for Li3(B11H14)(CB9H10)2 are obtained, respectively. LiB11H14 exhibits an oxidative stability limit of 2.6 V versus Li+/Li and the proposed decomposition products are discussed based on density functional theory calculations. Strategies are discussed to improve the stability of these compounds by modifying the chemical structure of the nido-hydroborate cage. Galvanostatic cycling in symmetric cells with two lithium metal electrodes shows a small overpotential increase from 22.5 to 30 mV after 620 h (up to 0.5 mAh cm−2), demonstrating that the electrolyte is compatible with metallic anodes. Finally, the Li2(B11H14)(CB11H12) electrolyte is employed in a proof-of-concept half cell with a TiS2 cathode with a capacity retention of 82% after 150 cycles at C/5.

DOI: https://doi.org/10.1002/adfm.202010046

ADVANCED FUNCTIONAL MATERIALS
www.afm-journal.de

Nido-Hydroborate-Based Electrolytes for All-Solid-State Lithium Batteries

SeyedHosein Payandeh, Daniel Rentsch, Zbigniew Łodziana,* Ryo Asakura, Laurent Bigler, Radovan Černý, Corsin Battaglia, and Arndt Remhof**

Hydroborate-based solid electrolytes have recently been successfully employed in high voltage, room temperature all-solid-state sodium batteries. The transfer to analogous lithium systems has failed up to now due to the lower conductivity of the corresponding lithium compounds and their high cost. Here $LiB_{11}H_{14}$ *nido*-hydroborate as a cost-effective building block and its high-purity synthesis is introduced. The crystal structures of anhydrous $LiB_{11}H_{14}$ as well as of $LiB_{11}H_{14}$-based mixed-anion solid electrolytes are solved and high ionic conductivities of 1.1×10^{-4} S cm^{-1} for $Li_2(B_{11}H_{14})(CB_{11}H_{12})$ and 1.1×10^{-3} S cm^{-1} for $Li_3(B_{11}H_{14})(CB_9H_{10})_2$ are obtained, respectively. $LiB_{11}H_{14}$ exhibits an oxidative stability limit of 2.6 V versus Li^+/Li and the proposed decomposition products are discussed based on density functional theory calculations. Strategies are discussed to improve the stability of these compounds by modifying the chemical structure of the *nido*-hydroborate cage. Galvanostatic cycling in symmetric cells with two lithium metal electrodes shows a small overpotential increase from 22.5 to 30 mV after 620 h (up to 0.5 mAh cm^{-2}), demonstrating that the electrolyte is compatible with metallic anodes. Finally, the $Li_2(B_{11}H_{14})(CB_{11}H_{12})$ electrolyte is employed in a proof-of-concept half cell with a TiS_2 cathode with a capacity retention of 82% after 150 cycles at C/5.

1. Introduction

Solid-state electrolytes combining liquid-like ionic conductivity, stability against metallic anodes, compatibility with high-voltage cathodes, processability, and low environmental impact and cost are essential for next-generation all-solid-state batteries (ASSBs). They promise to overcome the limitations of the current lithium-ion technology with higher power and energy density while improving operational safety.[1,2]

Currently, a few material classes exhibiting sufficiently high ionic conductivities are under consideration as potential candidates for the solid electrolyte of all-solid-state Li batteries: Ion-conducting oxides show moderate to high Li-ion conductivities on the order of 10^{-6} to 10^{-3} S cm^{-1} at room temperature.[3] They are hard, brittle materials that require sintering to minimize interface resistance and are vulnerable to crack formation and contact loss caused by volume changes during cycling.[4] Thiophosphates such as $Li_{10}GeP_2S_{12}$ ($\sigma = 12$ mS cm^{-1}) and Li_2S-P_2S_5 ($\sigma = 17$ mS cm^{-1}) exhibit liquid-like ionic conductivity at room temperature. Their limited chemical and electrochemical interface stability, however, require the use of protective coatings to form stable interfaces, hindering their integration into competitive batteries.[5,6] Halides such as Li_3YCl_6 and Li_3YBr_6, have recently shown high ionic conductivity >1 mS cm^{-1} at 25 °C and high oxidative stability up to 4 V versus Li^+/Li. However, they are unstable against Li metal and are typically used with a Li-In alloy or in two-layer combination with other electrolytes to stabilize the interface with Li metal.[7–9]

Dr. S. Payandeh, R. Asakura, Dr. C. Battaglia, Dr. A. Remhof
Laboratory of Materials for Energy Conversion
Empa
Swiss Federal Laboratories for Materials Science and Technology
Ueberlandstrasse 129, Dübendorf 8600, Switzerland
E-mail: Seyedhosein.payandeh@empa.ch; arndt.remhof@empa.ch

Dr. D. Rentsch
Laboratory of Functional Polymers
Empa
Swiss Federal Laboratories for Materials Science and Technology
Ueberlandstrasse 129, Dübendorf 8600, Switzerland

The ORCID identification number(s) for the author(s) of this article can be found under https://doi.org/10.1002/adfm.202010046.

DOI: 10.1002/adfm.202010046

Prof. Z. Łodziana
Institute of Nuclear Physics
Polish Academy of Sciences
ul. Radzikowskiego 152, Kraków 31-342, Poland
E-mail: zbigniew.lodziana@ifj.edu.pl

R. Asakura
Department of Physical Chemistry
University of Geneva
24 rue du Général-Dufour, Geneva 4 1211, Switzerland

Prof. L. Bigler
Department of Chemistry
University of Zurich
Winterthurerstrasse 190, Zurich 8057, Switzerland

Prof. R. Černý
Laboratory of Crystallography
Department of Quantum Matter Physics
University of Geneva
Quai Ernest-Ansermet 24, Geneva 4 1211, Switzerland

Solid polymer electrolytes composed of a Li salt dissolved into a polymer matrix are another class of solid-state Li-ion conductors. Due to their flexibility, low interfacial resistance, and low cost, they are still in the focus of many research activities, regardless of their low ionic conductivity, limited thermal range of operation and narrow electrochemical stability window.[10]

Recently, complex metal hydroborates, in particular, metal *nido*-/*closo*-hydroborates and carba-*closo*-hydroborates have emerged as promising alternative solid electrolytes,[11–14] providing liquid-like ionic conductivity,[15] stability against alkali metal anodes, and oxidative stability of up to 4 V versus Na^+/Na.[16–23] Furthermore, they show favorable mechanical properties[24] and are solution-processable, facilitating their integration in ASSB using slurry processes.[21]

Due to the proper matching size of the hydroborate anions with Na^+ cation and formation of discorded structures, the ionic conductivity of the Na-hydroborates usually surpasses the ones of their Li equivalents.[15,23,25,26] An ionic conductivity of ≈70 mS cm^{-1} at 27 °C has been obtained for $Na_2(CB_9H_{10})(CB_{11}H_{12})$ in this class of materials.[15] Stable 3 V cycling was demonstrated in Na-Sn/$NaCrO_2$ half cells with high cathode mass loadings of ≈7.7 mg cm^{-2}.[27] Moreover, some of us recently demonstrated stable 4 V room-temperature cycling of $Na/Na_3(VOPO_4)_2F$ all-solid-state cells for >800 cycles without any protective coatings.[28]

Currently, the most promising Li-ion solid electrolyte in the hydroborate family is $(1–x)LiCB_9H_{10}$–$xLiCB_{11}H_{12}$ (x = 0.1–0.9) which is stable against Li metal and shows high ionic conductivity of 6.9×10^{-5}–6.7×10^{-3} S cm^{-1} at 25 °C.[15,18,29] However, $LiCB_9H_{10}$ is challenging to synthesize and therefore rather expensive with a price >120 000 € kg^{-1}, hindering a broader application of this material.[30]

In this study, we propose the use of the *nido*-hydroborate (lithium tetradecahydroundecaborate, $LiB_{11}H_{14}$) as a cost-effective replacement of $LiCB_9H_{10}$ as the $B_{11}H_{14}^-$ anion exhibits the same charge and similar size as the $CB_9H_{10}^-$ anion. First, we describe the synthesis and purification of solvent-free $LiB_{11}H_{14}$ and we solve its crystal structure. Several impurity side products are thoroughly identified using ^{11}B nuclear magnetic resonance spectroscopy (NMR) and electrospray ionization high-resolution mass spectrometry (ESI-MS). Second, *nido*-hydroborate-based electrolytes are formed by mixing $LiB_{11}H_{14}$ with *closo*-hydroborates and carba-*closo*-hydroborates, such as $Li_2B_{12}H_{12}$, $LiCB_{11}H_{12}$, and $LiCB_9H_{10}$ and their crystal structures and electrochemical properties are investigated. Finally, *nido*-hydroborate-based electrolytes are evaluated in a proof-of-concept battery with a Li metal anode and a TiS_2 cathode. Our results show economic viability of hydroborate electrolytes for all-solid-state lithium batteries.

2. Results and Discussion

2.1. Synthesis and Impurity Identifications of Novel *Nido*-Hydroborates

2.1.1. Experimental Procedure to Synthesize Solvent-Free $LiB_{11}H_{14}$

$LiB_{11}H_{14}$ was synthesized based on the reaction of *n*-butyllithium (LiC_4H_9, BuLi) with $(CH_3)_3NHB_{11}H_{14}$ in tetrahydrofuran (THF)solution according to Equation (1)

$$(CH_3)_3NHB_{11}H_{14}(sol) + LiC_4H_9(susp) \xrightarrow{THF,\ 25\ °C} LiB_{11}H_{14}(sol) + (CH_3)_3N(g) + C_4H_{10}(g) \quad (1)$$

After THF was removed, water was added to filter unreacted, insoluble $(CH_3)_3NHB_{11}H_{14}$, resulting in an aqueous solution of $LiB_{11}H_{14}(H_2O)_n$ ($1 < n < 2$). The complete removal of the coordinated water without decomposition of the $B_{11}H_{14}^-$ cage is challenging. Our initial attempts using heat treatment led to the formation of $LiB_{11}H_{13}R$ impurities (R = OH, $OB_{11}H_{13}Li$, O-Butyl(O-Bu)) and $LiB_{11}H_{12}O$ (Samples **A**–**D**, Table S1, Supporting Information). **Figure 1**a shows the open-cage molecular structure of the *nido*-hydroborate anion. The impurities were identified by $^{11}B\{^1H\}$ NMR (see Figure 1b; and Table S1 (Supporting Information); for discussion, see Section 2.2 below).

The synthesis of pure $LiB_{11}H_{14}$ was made possible by using an excess of *n*-butyllithium in the synthesis (Equation (1)). This leads to a partial reduction of the sample, resulting in a mixture of $LiB_{11}H_{14}$ and $Li_2B_{11}H_{13}$. After heat treatment under aqueous conditions, $Li_2B_{11}H_{13}$ converted back to $LiB_{11}H_{14}$ according to Equation (2), allowing the synthesis of solvent-free $LiB_{11}H_{14}$ (Figure 1c)

$$Li_2B_{11}H_{13}(sol) + H_2O(l) \xrightarrow{80–100\ °C} LiB_{11}H_{14}(s) + LiOH(s) \quad (2)$$

It is important to mention that H_2 is released for the synthesis of $(CH_3)_3NHB_{11}H_{14}$ as a precursor.[13][31] Therefore, H_2 release during the synthesis should be considered for the large-scale production of these materials. However, similar compounds such as $M_2B_{12}H_{12}$ (M = Li, Na) in which H_2 is released during the synthesis are commercialized and produced on a kg scale.[32]

Figure 1c displays the respective $^{11}B\{^1H\}$ NMR spectra. The complete removal of water was evidenced by powder X-ray powder diffraction (PXRD), IR spectroscopy, and thermogravimetric analysis (TGA, see Figures S1 and S2, Supporting Information). In the last step, $LiB_{11}H_{14}$ is separated by adding THF to the mixture to filter THF-insoluble LiOH and by subsequent drying at 100 °C for 16 h to remove THF. This procedure also allows the removal of coordinated water from commercial $LiB_{11}H_{14}(H_2O)_n$ samples and is described in more detail in the Supporting Information (Samples **E**, **G**). Finally, anion mixing was used as a known strategy to improve ionic conductivity.[15,33] The pure $LiB_{11}H_{14}$ was ball-milled with $LiCB_9H_{10}$, $LiCB_{11}H_{12}$, or $Li_2B_{12}H_{12}$ in different molar ratios (Table S1, Supporting Information). The compositions of the samples were determined by peak shape analysis of the 1D ^{11}B NMR spectra. The results are summarized in Table S1 (Supporting Information). We found that $LiB_{11}H_{14}$ partially decomposed during the ball-milling process. This leads to the formation of nonassignable resonances in the ^{11}B NMR data (Table S1 and Figure S3, Supporting Information).

2.1.2. Identification of $LiB_{11}H_{13}R$ By-Products of $LiB_{11}H_{14}$ Synthesis

$LiB_{11}H_{14}$ (1): The molecular structure of **1** depicted in Figure 1a has been fully determined previously in ref. [13] It can be described as an oblate spheroid with the minor axis (the "height") perpendicular to the opening of the nest of 4.6 Å and a major axis (the "width" or the "diameter") of 5.3 Å (**Figures 2** and **3**a).

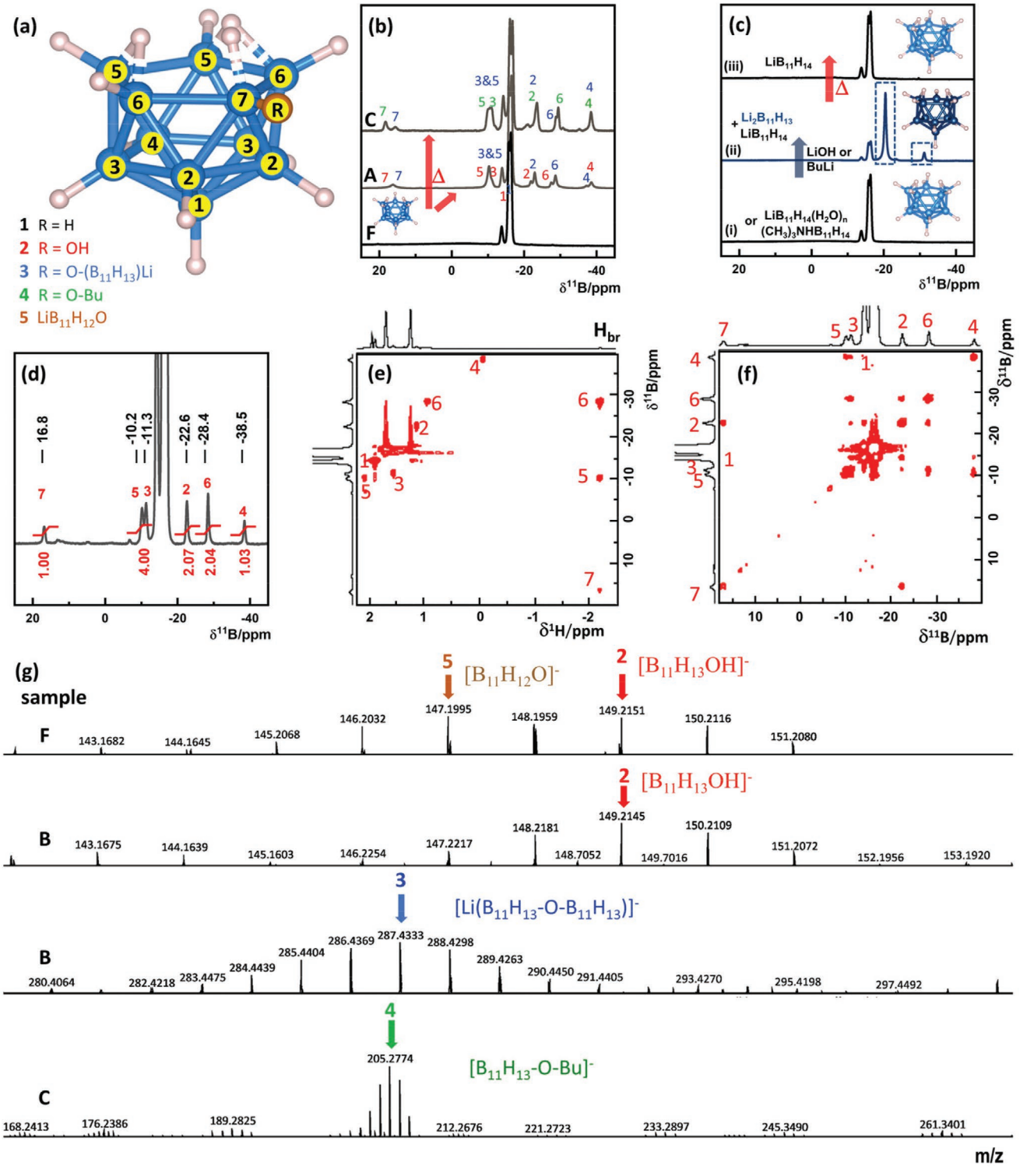

Figure 1. a) General chemical structure with the labeling of boron atoms of the *nido*-hydroborate anions $LiB_{11}H_{13}R$ 1–4 (R in 1 = H, 2 = OH, 3 = $O(B_{11}H_{13})Li$, 4 = O-Bu), 5 = $LiB_{11}H_{12}O$. b) $^{11}B\{^1H\}$ NMR spectra of $LiB_{11}H_{14}(H_2O)_n$ and $LiB_{11}H_{13}R$ after heat treatment under different conditions. The boron resonances of species 2, 3, and 4 are assigned by red, blue, and green numbers. c) $^{11}B\{^1H\}$ NMR spectra of i) the precursors $(CH_3)_3NHB_{11}H_{14}$ or $LiB_{11}H_{14}(H_2O)_n$, (bottom), ii) the mixture of $LiB_{11}H_{14}$ and $Li_2B_{11}H_{13}$ in basic solutions (middle), and (iii) of pure $LiB_{11}H_{14}$ after heat treatment (top). d) $^{11}B\{^1H\}$, e) ^1H-^{11}B HSQC, and f) ^{11}B-$^{11}B\{^1H\}$ COSY NMR spectra with the assignment of resonances to the chemical structure of 2 in Sample F. Please note that the signals of the starting material 1 account to ≈93 mol% of the total signal intensity. The NMR spectra shown in b,c) are recorded in THF and d–f) in CD_3CN solutions. g) Expanded regions of interest of the (–)-ESI-MS with $^{11}B/^{10}B$ isotopic patterns assigned to 2–5 for Samples B, C, and F.

$LiB_{11}H_{13}OH$ (2): The chemical structures of the above-mentioned impurities, which were formed during the drying process (Samples, **B**, **C**, and **F**; see Table S1, Supporting Information), were unveiled using NMR and MS (Figure S4 and Table S2, Supporting Information). The 1D and 2D ^{1}H and ^{11}B NMR data of Sample **F** leads to the identification of $LiB_{11}H_{13}OH$ (**2**) as a first by-product as shown in Figure 1d–f. Besides the strong resonances of the starting material, six distinct signals with an intensity ratio of 1:2:2:2:2:1 are observed in the 1D ^{11}B NMR spectrum (Figure 1d) and in the ^{1}H-^{11}B HSQC NMR spectrum, each of these resonances results in a distinct cross peak assigned to positions 2–7 of the chemical structure (Figure 1a). Note that the cross signal of position 1 in the spectrum is hidden beyond the strong resonances of $LiB_{11}H_{14}$ (**1**). The bridging protons H_{br} of $LiB_{11}H_{13}OH$ at the open apex correlate to boron resonances at 16.9, –10.2, and –28.4 ppm (Figure 1e), which therefore can be assigned to positions 5–7 of the chemical structure (Figure 1a, bonds of protons H_{br} are shown with dashed lines). From ^{11}B NMR chemical shift reasons and the relative signal intensity, the resonance at 16.9 ppm can be assigned to B7. Position B2 was assigned from the cross peak between the boron resonances at 16.9 and –22.6 ppm in the ^{11}B-^{11}B correlated NMR spectrum (Figure 1f). The cross peak at –14.3/–22.6 ppm observed in the ^{11}B-^{11}B correlated NMR spectrum leads to the unambiguous identification of B1, which was hidden beyond strong resonances of the starting material in the other 1D and 2D NMR data. Subsequently, all ^{1}H and ^{11}B NMR chemical shifts of the molecule were assigned (for enlarged regions of ^{1}H-^{1}H and ^{11}B-^{11}B correlated NMR spectra see Figure S6, Supporting Information). The presence of an OH group in **2** (in Sample **F**) was confirmed by the correlation observed at 4.00 ppm to the bridging protons H_{br} at –2.21 ppm in the ^{1}H-^{1}H correlated NMR spectrum (Figure S6e, Supporting Information). All other observable ^{1}H-^{1}H correlations originate from ^{2}J or ^{3}J couplings and support the signal assignments to the chemical structure of the boron cage shown in Figure 1a. Please note that the boron—boron bonds of B2—B2, B5—B5, and B6—B7 could not be verified to fully identify the boron cage. For reasons of symmetry, the boron atoms in the first two cases are homotopic and therefore have identical ^{11}B NMR chemical shifts, and relaxation reasons may be responsible for the missing B6—B7 cross peak (see, e.g., [34–36]).

The presence of $LiB_{11}H_{13}OH$ (**2**) in Samples **B** and **F** was further confirmed by their corresponding mass spectra (Figure 1g).[37] The $^{11}B/^{10}B$ isotopic patterns with the most abundant signals at m/z 149.215 are assigned to the molecular composition of $B_{11}H_{13}OH^-$. A calculated MS pattern is presented in Figure S7 (Supporting Information) to confirm the assignment to $B_{11}H_{13}OH^-$ and the summary of all MS data is given in Table S2 (Supporting Information).

$Li_2(B_{11}H_{13}$-O-$B_{11}H_{13})$ (3): For each of the ^{11}B NMR resonances assigned to **2**, a 2nd signal at almost identical chemical shift is observed in Sample **B** (see Figure 1b). The decisive deviation in the NMR data of this new species (**3**) is the complete absence of an OH resonance in the ^{1}H NMR spectrum. Nevertheless, the chemical structures of **2** and **3** must be rather similar, since only small deviations of the ^{1}H and ^{11}B NMR chemical shifts can be observed for the two species (Figure 1b; and Figure S8, Supporting Information). In the spectral region showing the resonances of bridging protons H_{br} of the diffusion-edited ^{1}H NMR spectrum (Figure S9a, Supporting Information), the signal of **2** is considerably reduced with increasing gradient strengths compared to the resonance of **3**. This indicates that **3** diffuses less rapidly and must probably have a higher molecular weight than **2**. In the mass spectrum of Sample **B**, the most abundant signal of the $^{11}B/^{10}B$ isotopic pattern centered at m/z 287.433 can be assigned to the sum formula $B_{22}H_{26}LiO^-$ ($Li(B_{11}H_{13}$-O-$B_{11}H_{13})^-$) (Figure 1g; and Figure S10, Supporting Information). Additionally, the peak pattern observed for Samples **B** and **C** with only 0.5 mass units distances of the isotopic peaks and the most abundant mass peak centered at m/z 140.209 (Figure S11, Supporting Information) can be assigned to the double-charged anions of **3**, with the molecular formula $B_{22}H_{26}O^{2-}$. This finding confirms the hypothesis from the NMR data that **3** should have a similar molecular composition but a higher molecular weight than **2**. The formation of a dimer with a bridging oxygen seems not to be uncommon for *closo*-hydroborates as it has been previously observed for other species such as $[B_{10}H_{13}$-O-$B_{10}H_{13}]$.[38]

$Li(B_{11}H_{13}$-O-Bu) (4): For species **4**, the ^{1}H-^{11}B and ^{11}B-^{11}B correlated 2D NMR data (Figure S12, Supporting Information) suggest a boron—boron network similar to the data evaluated for **2** and **3**. In the ^{1}H and ^{13}C NMR spectra (Figure S13, Supporting Information) resonances assignable to an *O-n*-butyl (O-Bu) group were identified. For chemical shift reasons, the signal at 70.7 ppm in the ^{13}C NMR spectrum can be assigned to an *n*-butyl ether residue, but NMR data further suggest that **4** consists of a $B_{11}H_{13}$ core unit with an attached butoxy group at the open apex boron. This was confirmed by mass spectrometry of Sample **C** with a prominent $^{11}B/^{10}B$ isotopic pattern with the most abundant signal at m/z 205.277, corresponding to the molecular formula $B_{11}H_{13}$-O-Bu^- ($B_{11}H_{22}C_4O^-$) (Figure 1g; and Figure S14, Supporting Information). As already observed in the case of Sample **B** (a mixture of **2** and **3**), in the diffusion-edited ^{1}H NMR spectrum of Sample **C** (Figure S9b, Supporting Information) the signal of **4** is significantly reduced with increasing gradient strengths compared to the resonance of **3**, which is associated with the lower molecular weight of **4** compared to **3**. It is important to mention that the formation of compound **4** was observed only when $LiB_{11}H_{14}(H_2O)_n$ is heat-treated in THF. Heat treatment of $LiB_{11}H_{14}$ in THF did not form compound **4**, suggesting that the coordinating water plays a role in C—O bond scission of tetrahydrofuran and its attachment to the boron cage. The formation of **4** was reinvestigated in presence of THF-d_8 as a reactant. From the 1D and 2D ^{1}H, ^{2}H, ^{11}B, and ^{13}C NMR data (see Figure S15 and discussion in the Supporting Information part), we unequivocally identified O-CD_2-CD_2-CD_2-CD_2H as the butoxy residue of **4**.

$LiB_{11}H_{12}O$ (5): Besides the impurities **1–4** discussed above, a tiny amount of a further impurity was observed in Sample **F**. In this sample, in addition to the resonances of **1** and **2**, cross-peaks of a minor by-product assignable to $LiB_{11}H_{12}O$ (**5**) were observed in the ^{1}H-^{11}B HSQC NMR spectrum of Sample **F** when a very low threshold was applied (Figure S16, Supporting Information). All ^{1}H and ^{11}B NMR data of this species are very similar to the data described in ref. [34,35] This assignment was further supported by the mass spectrum of Sample **F**

(Figure 1g; and Figure S7, Supporting Information), with the most abundant signal of the $^{11}B/^{10}B$ isotopic pattern at m/z 147.199, which is associated the sum formula of $B_{11}H_{12}O^-$ (**5**).

An overview of the ^{11}B NMR spectra with integrated regions of selected samples is presented in Figure S17 (Supporting Information) and global assignments of ^{11}B NMR chemical shift regions of compounds **1–5** are shown in Table S3 (Supporting Information). Besides, the ground state energy of different isomers of $B_{11}H_{13}OH^-$ (**2**), $(B_{11}H_{13}\text{-}O\text{-}B_{11}H_{13})^{2-}$ (**3**), and $B_{11}H_{12}O^-$ (**5**) are calculated and shown in Figure S18 (Supporting Information). For $B_{11}H_{13}OH^-$ and $(B_{11}H_{13}\text{-}O\text{-}B_{11}H_{13})^{2-}$, the energy differences between isomers are relatively small (≈0.1–0.2 eV) but the most stable isomers show the same configurations predicted by NMR. For $B_{11}H_{12}O^-$, the oxygen at the open vertex is far more stable than in other positions, confirming the NMR results. Note that the presence of oxygen at other positions might lead to a major change of anion structure.

Understanding the chemical composition of the impurities is the basis to establish a high purity synthesis method for $LiB_{11}H_{14}$, as discussed earlier. In the next sections, the effect of anion mixing (including the impurities) on the crystal structures and ionic conductivities are discussed. Moreover, the effect of impurities on the electrochemical stabilities of the compounds is investigated using density functional theory (DFT) calculations.

2.2. Crystal Structures of the Compounds

In the next step, the crystal structures of $LiB_{11}H_{14}$ and of the anion mixed compounds ($LiB_{11}H_{14}$:$Li_2B_{12}H_{12}$ (1:1), $LiB_{11}H_{14}$:$LiCB_{11}H_{12}$ (1:1, 1:2, 2:1), and $LiB_{11}H_{14}$:$LiCB_9H_{10}$ (1:2) were solved by means of PXRD.

The crystal structure of the low temperature (LT) $LiB_{11}H_{14}$ was solved in an orthorhombic unit cell with space group *Pbca* and cubic-close packing (ccp) of the $B_{11}H_{14}^-$ anions and was optimized by DFT (Figures S19, S20a, and S22, Supporting Information). Unlike tetrahedral coordination of Na in $NaB_{11}H_{14}$,[13] Li^+ ions in this structure lie in trigonal planar sites formed by three $B_{11}H_{14}^-$ anions and located between octahedral and tetrahedral sites (Figure 2b). Trigonal planar coordination of Li has been also observed for other Li salts of hydroborates, such as $Li_2B_{12}H_{12}$ [39] and $Li_2B_{10}H_{10}$.[40] In general, the preferred coordination environment of the cation is defined based on the cation-to-anion size ratio and by using the first Pauling rule (Table S4, Supporting Information).[41,42] Taking 0.73 Å as the size of Li^+ (crystal radius in tetrahedral coordination[43]) and 4.6 Å as the estimated size of the $B_{11}H_{14}^-$ anion (apical axis, Figure 3a), the cation-to-anion size ratio is ≈0.16, suggesting triangular coordination.[41] However, in $NaB_{11}H_{14}$ with a larger cation (Na^+ ≈1.13 Å), crystal radius in tetrahedral coordination,[43]), the cation/anion size ratio increases to ≈0.25, and tetrahedral coordination is preferred for Na^+ ions. Similarly to $NaB_{11}H_{14}$, the $B_{11}H_{14}^-$ anion in LT-$LiB_{11}H_{14}$ is oriented with the open side of the cage away from the Li^+ cation. This preferred orientation is explained by the more negative closed side of the cage that interacts with the cation (Figure 3b). A comparable trend has been observed for $CB_{11}H_{12}^-$ and $CB_9H_{10}^-$ in which the anions are oriented so that the considerably more positive

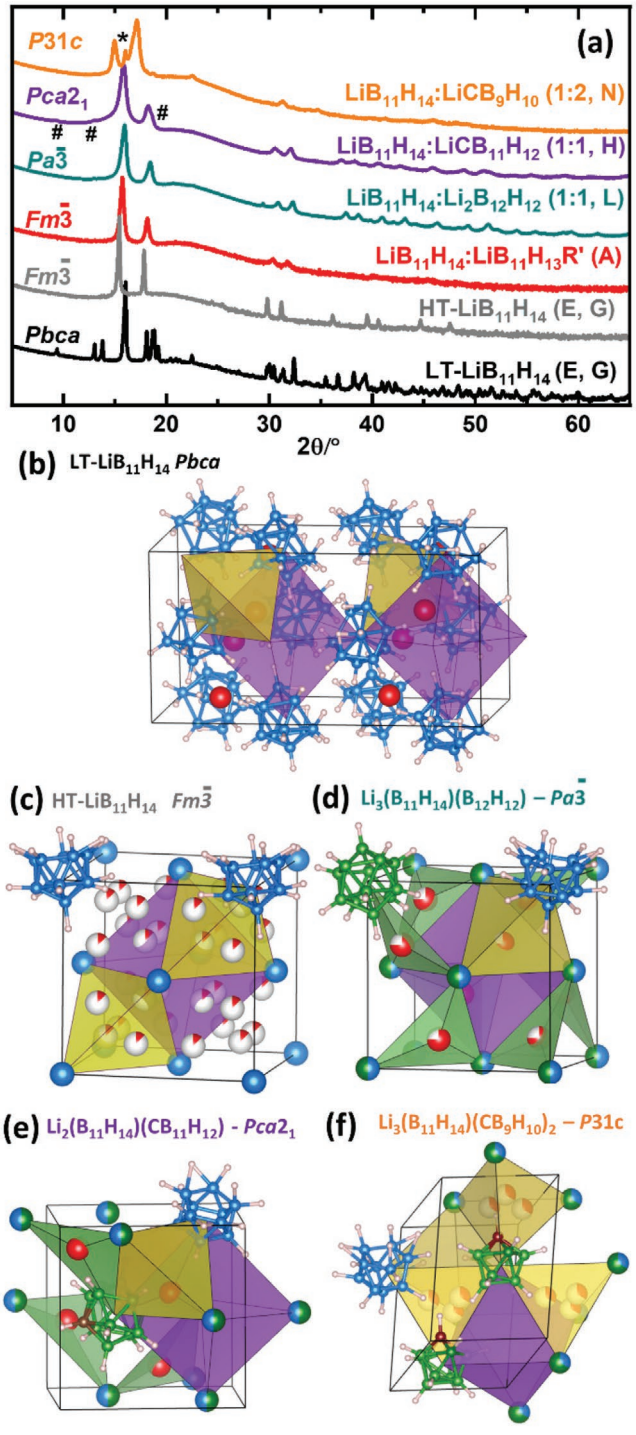

Figure 2. a) PXRD patterns of the LT and HT phases of $LiB_{11}H_{14}$ and mixtures of $LiB_{11}H_{14}$:$LiB_{11}H_{13}R'$ (R' = OH and $OB_{11}H_{13}Li$), $LiB_{11}H_{14}$:$Li_2B_{12}H_{12}$ (1:1), $LiB_{11}H_{14}$:$LiCB_{11}H_{12}$ (1:1), $LiB_{11}H_{14}$:$LiCB_9H_{10}$ (1:2) in a logarithmic scale (λ_{Cu}). Crystal structures of b) LT and c) HT phases of $LiB_{11}H_{14}$, d) $Li_3(B_{11}H_{14})(B_{12}H_{12})$, e) $Li_2(B_{11}H_{14})(CB_{11}H_{12})$, and f) $Li_3(B_{11}H_{14})(CB_9H_{10})_2$. # and * indicate the characteristic Bragg reflections of the $Pca2_1$ phase and of the remaining $LiB_{11}H_{14}$, respectively. B atoms in the crystal structures are represented by green and blue (for $B_{11}H_{14}^-$) spheres, and H and Li atoms are represented by gray and red spheres, respectively.

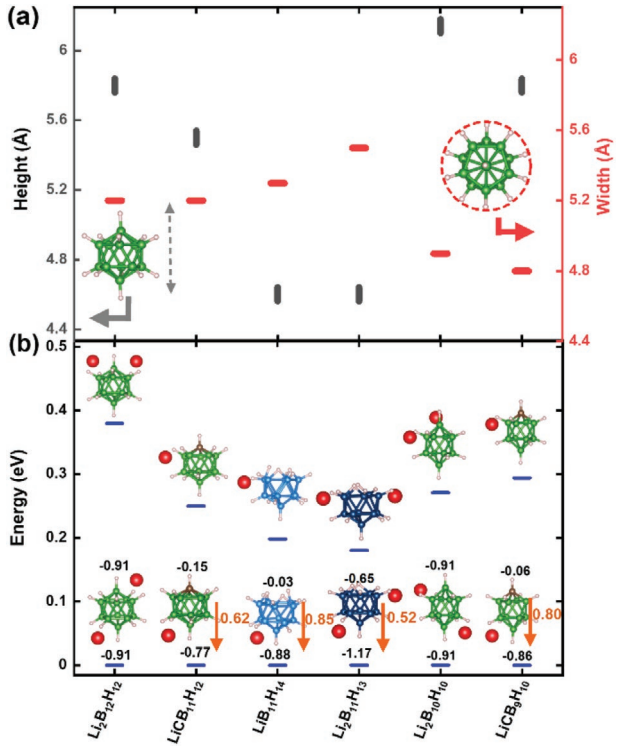

Figure 3. a) Approximate relative sizes of the hydroborates anions. The height and width of the hydroborate anions are shown by gray and red bars, respectively. b) Calculated Bader charges and Li configuration for the hydroborates in the ground and least stable states. B, H, and Li atoms are represented by green, gray, and red spheres, respectively. B atoms for the $B_{11}H_{14}^-$ and $B_{11}H_{13}^{2-}$ are presented in a light and dark blue, respectively. Orange arrows indicate the dipole moments.

C-bonded H atom avoids proximity to the neighboring cations (Figure 3b).[44,26] Upon heating, $LiB_{11}H_{14}$ undergoes a phase transition at ≈112 °C to a cubic phase with the $Fm\bar{3}$ space group and ccp packing of the anions similar to high temperature (HT) phases of $Li_2B_{12}H_{12}$ and $LiCB_{11}H_{12}$ (Figure 1c; and Figure S2b, Supporting Information).[44,45]

The coordination environment of Li remains trigonal planar and 3D conduction channels appear to form for the Li^+ cations in ccp anion packing (Figure S20b, Supporting Information). The Li^+ jumps between tetrahedral and octahedral sites occur through the shared faces where Li^+ is localized in a disordered manner (Figure S21a, Supporting Information).[46] Preliminary DFT calculations of the conduction mechanism show Li^+ hopping near the vicinity of tetrahedral sites, and large $Li^+ - Li^+$ correlations in electrolytes containing a fraction of $CB_9H_{10}^-$. This points out to lower activation energy of mixed anion compounds (Figure S21b, Supporting Information) Ion conduction mechanism of related compounds is discussed in detail.[47]

The sizes and polarities of the hydroborate anions under discussion are summarized in Figure 3. The charges were calculated in the simplified systems that consider one isolated hydroborate anion and cations compensating the charge of the anion. This model neglects the periodic crystal structure; however, it allows observation of the charge redistribution on the anions related to the motion of Li. When $LiB_{11}H_{14}$ is mixed with the bigger anions of $Li_2B_{12}H_{12}$ and $LiCB_{11}H_{12}$ (Samples **H**–**L**), solid solutions form, and a $B_{11}H_{14}^-$ anion integrates into the LT crystal lattice of $Li_2B_{12}H_{12}$ and $LiCB_{11}H_{12}$.[39,44] Therefore, $Li_3(B_{11}H_{14})(B_{12}H_{12})$ crystallizes in the $Pa\bar{3}$ space group and $Li_2(B_{11}H_{14})(CB_{11}H_{12})$, $Li_3(B_{11}H_{14})(CB_{11}H_{12})_2$, and $Li_3(B_{11}H_{14})_2(CB_{11}H_{12})$ crystallize in the $Pca2_1$ space group (Figure 2d,e; and Figure S23, Supporting Information). Both structures have the ccp packing of the anions and triangular coordination for Li.

In the case of mixing $LiB_{11}H_{14}$ with $LiCB_9H_{10}$ as an example for a smaller anion (Samples **M**, **N**), the HT phase of $LiCB_9H_{10}$ with a hexagonal unit cell and with the space group $P\bar{3}1c$ is stabilized. This is confirmed by the disappearance of the Bragg reflection at $2\theta = 8.6°$ for the LT phase and appearance of a shoulder at $2\theta = 16.6°$ for the HT phase (red and green arrows in Figure S24, Supporting Information).[15,25] In this structure, Li atoms occupy tetrahedral sites sharing a face with an empty octahedral site (Figure 2f). The higher coordination of lithium is based on the smaller size of anions used in this compound and is in favor of Li-ion conductivity (based on the Pauling rule, Table S4, Supporting Information).[42]

In addition, the presence of small amount of impurities $LiB_{11}H_{13}R'$ (R' = OH, $B_{11}H_{13}OLi$) in $LiB_{11}H_{14}$ formed upon drying of $LiB_{11}H_{14}(H_2O)_n$ stabilizes the HT cubic phase of $LiB_{11}H_{14}$ with space group $Fm\bar{3}$ (Sample **A**). The diffraction pattern of this phase ($Fm\bar{3}$) is very similar to the orthorhombic $Pca2_1$ phase. These two patterns are distinct by the absence of the shoulder at $2\theta = 18.6°$ and some smaller reflections at $2\theta = 9.2, 12.9°$ for the cubic phase (Figure 2a). Structural parameters of the new compounds determined by Rietveld refinements are summarized in **Table 1**. The atomic coordinates of all solved structures are presented in Tables S8–S12 (Supporting Information).

2.3. Thermal Behavior

Figure 4a shows the thermal behavior of $LiB_{11}H_{14}$ and the mixed hydroborate compounds as observed by differential scanning calorimetry. The reversible phase transition from the orthorhombic to the cubic phase of $LiB_{11}H_{14}$ appears upon heating as an endothermic peak at ≈112 °C (Figure 4a,b; and Figure S26c, Supporting Information). Upon cooling, $LiB_{11}H_{14}$ transforms back to the orthorhombic phase with an exothermic event at ≈96 °C. Thermo-gravimetric measurements of $LiB_{11}H_{14}$ show an ≈3% weight loss at ≈180 °C (Figure S2b, Supporting Information), indicative of sample decomposition. Moreover, with prolonged heat treatment at 120 °C, the sample color changes from white to yellow and extra resonances in the ^{11}B NMR spectra appear, indicating thermal instability of $LiB_{11}H_{14}$ above the phase transition (Figure S25, Supporting Information). The decreased signal intensity in the ^{11}B NMR spectra indicates the insolubility of the decomposition products, indicative of the formation of dimers or poly-hydroborates with higher molecular masses.[48,49] The phase-transition temperature of $LiB_{11}H_{14}$ at 112 °C is lower than the ones of $Li_2B_{10}H_{10}$ and $Li_2B_{12}H_{12}$ (367 and 355 °C, respectively),[40,50] and is comparable to the phase-transition temperature of $LiCB_{11}H_{12}$ at ≈122 °C.[44]

For the $LiB_{11}H_{14}$:$Li_2B_{12}H_{12}$ (1:1, Sample **L**) mixture, an irreversible endothermic event is observed at T ≈120 °C for the first heating cycle. In the subsequent cycle, this event shifts to a lower temperature and fades (Figure 4a; and

Table 1. Structural data extracted from Rietveld refinements of the PXRD data.

Formula	Space group	T [°C]	Crystal system	Anion packing	Lattice parameters	V [Å^3]	Z	V/Z [Å^3]	ρ[g cm^{-3}]	Sample
$LiB_{11}H_{14}$	*Pbca*	25	Orthorombic	ccp	a = 9.8059 (3) b = 9.5118 (3) c = 18.8659 (6)	1759.66 (9)	8	219.96	1.06	**E**, **G**
$LiB_{11}H_{14}$	$Fm\bar{3}$	140	Cubic	ccp	a = 9.9465(6)	984.04(17)	4	246.01	0.94	**E**, **G**
$Li_3(B_{11}H_{14})(B_{12}H_{12})$	$Pa\bar{3}$	25	Cubic	ccp	a = 9.6219 (3)	890.80 (8)	4	222.7	1.10	**L**
$Li_2(B_{11}H_{14})(CB_{11}H_{12})$	$Pca2_1$	25	Orthorombic	ccp	a = 9.710(5) b = 9.551(5) c = 9.752(5)	904.3(8)	4	226.1	1.06	**H**
$Li_3(B_{11}H_{14})(CB_{11}H_{12})_2$	$Pca2_1$	25	Orthorombic	ccp	a = 9.680(3) b = 9.525(3) c = 9.764(3)	900.3(5)	4	225.1	1.08	**I**
$Li_3(B_{11}H_{14})_2(CB_{11}H_{12})$	$Pca2_1$	25	Orthorombic	ccp	a = 9.691(8) b = 9.517(7) c = 9.737(9)	898.0(13)	4	224.5	1.06	**J**
$Li_3(B_{11}H_{14})(CB_9H_{10})_2$	*P*31*c*	25	Trigonal	hcp	a = 6.8247(10) b = 10.610(3)	427.97(17)	2	213.9	1.02	**N**

Figure S26c, Supporting Information). We attribute this to the phase transition of the remaining unreacted $LiB_{11}H_{14}$ in the sample that could not be distinguished by PXRD and is dissolving in the $Li_2B_{12}H_{12}$ crystal lattice upon heating. For the $LiB_{11}H_{14}$:$LiCB_{11}H_{12}$ (1:1) mixtures (Sample **H**), the phase transition to the HT phase is observed at ≈80 °C (Figure 4a; and Figures S26 and S27, Supporting Information). In this system, the phase-transition temperature is dependent on the $LiB_{11}H_{14}$/$LiCB_{11}H_{12}$ ratio. Higher content of $LiB_{11}H_{14}$ decreases the phase transition to 70 °C for $LiB_{11}H_{14}$:$LiCB_{11}H_{12}$ (2:1, Sample **J**), while the higher content of $LiCB_{11}H_{12}$ increases the phase transition to ≈110 °C for $LiB_{11}H_{14}$:$LiCB_{11}H_{12}$ (1:2, Sample **I**) respectively (Figure S26d, Supporting Information).

In the mixtures $LiB_{11}H_{14}$:$LiB_{11}H_{13}R'$ (R' = OH, $OB_{11}H_{13}Li$) and $LiB_{11}H_{14}$:$LiCB_9H_{10}$, the HT phases are stabilized at room temperature and the phase transitions are completely suppressed (Figure 4; and Figure S26b,e, Supporting Information) which is similarly observed for other mixed anion systems.[13,15–17,33,51]

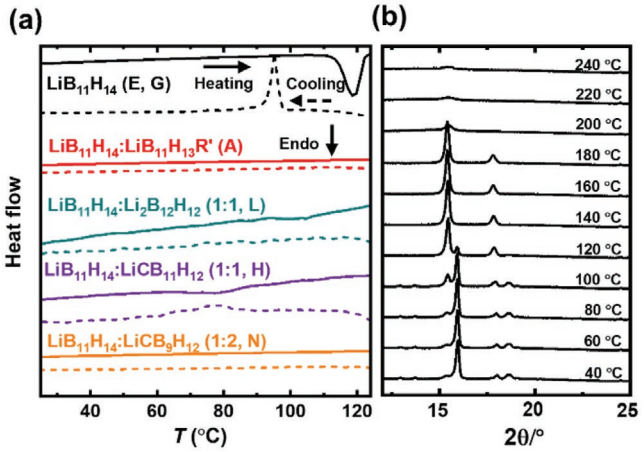

Figure 4. a) Differential scanning calorimetry of the samples (third cycle, $\Delta T/\Delta t$ = 5 °C min^{-1}). R' = OH, $B_{11}H_{13}OLi$. b) Temperature-dependent PXRD patterns of $LiB_{11}H_{14}$ (λ_{Cu}).

2.4. Conductivity

Figure 5 displays the temperature-dependent lithium-ion conductivity of the synthesized compounds. For comparison, the conductivities of $Li_2B_{12}H_{12}$, $LiCB_{11}H_{12}$, and $LiCB_9H_{10}$ are also presented. $LiB_{11}H_{14}$ shows a conductivity of 1.5 × 10^{-6} S cm^{-1} at 25 °C which is similar to the reported conductivity of $LiCB_{10}H_{13}$, but higher than the published data for $LiCB_9H_{10}$, $LiCB_{11}H_{12}$, and $Li_2B_{12}H_{12}$.[14,25,44,52,53] The apparent activation energy for $LiB_{11}H_{14}$ is 0.81 eV (Sample **E**) at low temperatures and reduces to 0.16 eV above the phase transition at ≈112 °C (Figures S28a and S29, Supporting Information).

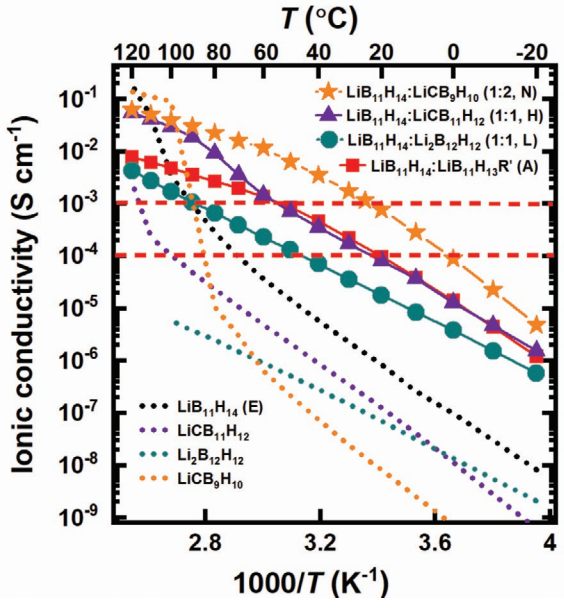

Figure 5. Arrhenius plots of the lithium-ion conductivity of $LiB_{11}H_{14}$, $Li_2B_{12}H_{12}$, $LiCB_{11}H_{12}$, $LiCB_9H_{10}$, and mixtures of $LiB_{11}H_{14}$:$LiB_{11}H_{13}R'$, $LiB_{11}H_{14}$:$Li_2B_{12}H_{12}$ (1:1), $LiB_{11}H_{14}$:$LiCB_{11}H_{12}$ (1:1), and $LiB_{11}H_{14}$:$LiCB_9H_{10}$ (1:2). The red dash lines indicate σ = 10^{-4} and 10^{-3} S cm^{-1}.

For the $LiB_{11}H_{14}$:$LiCB_{11}H_{12}$ solid solutions (Samples **H–K**), the conductivity depends on the $LiB_{11}H_{14}$:$LiCB_{11}H_{12}$ ratio (Figure S28, Supporting Information). The conductivity of 1.1×10^{-4} S cm^{-1} at 25 °C is observed for the 1:1 mixture. The jump in the conductivity at ≈80 °C corresponds to the phase transition to the cubic HT phase (Figure S27, Supporting Information). The $LiB_{11}H_{14}$:$Li_2B_{12}H_{12}$ (1:1, Sample **L**) solid solution shows lower conductivity of $\approx 2.3 \times 10^{-5}$ S cm^{-1} at 25 °C, which could be ascribed to nonpolarity of $B_{12}H_{12}^{2-}$ and its bivalent charge that increases the Li content in the $Li_3(B_{11}H_{14})(B_{12}H_{12})$ structure.

The $LiB_{11}H_{14}$:$LiB_{11}H_{13}R'$ (R' = OH and $OB_{11}H_{13}Li$, Sample **A**) in which the presence of impurities stabilizes the HT cubic phase of $LiB_{11}H_{14}$ ($Fm\bar{3}$), shows an ionic conductivity of 1.5×10^{-4} S cm^{-1} at 25 °C. The highest ionic conductivity of 1.1×10^{-3} S cm^{-1} within this system is obtained for the $LiB_{11}H_{14}$:$LiCB_9H_{10}$ (1:2, Sample **N**) mixture where the disordered HT hexagonal unit cell of $LiCB_9H_{10}$ is stabilized. The PXRD pattern of this sample still shows the presence of unreacted $LiB_{11}H_{14}$ and suggests tuning the $LiB_{11}H_{14}$:$LiCB_9H_{10}$ ratio to obtain higher conductivity (Figure 2a; and Figures S24b and S27, Supporting Information). A non-Arrhenius conductivity behavior is observed for both $LiB_{11}H_{14}$:$LiB_{11}H_{13}R'$ and $LiB_{11}H_{14}$:$LiCB_{11}H_{12}$ samples, where the HT disordered phases are stabilized. This is the characteristic behavior of disordered structures in hydroborates and has been observed in former studies.[13,15,17] A transition from a low-temperature regime with a correlated cationic motion to a high-temperature regime with noncorrelated cationic diffusion has been suggested to be responsible for this behavior.[54] The conductivity trends indicate that small, single charged anions with high polarity are required to form suitable conduction channels for Li^+ cations and to obtain high conductivities in Li-hydroborates. Although $B_{11}H_{14}^-$ and $CB_9H_{10}^-$ have similar sizes and polarities (Figure 3), the prolate (elongated) shapes of the $CB_9H_{10}^-$ anion appear to be more favorable for Li^+ conduction pathways by stabilizing the disordered hexagonal unit cell. However, the synthesis of $CB_9H_{10}^-$ is challenging and the use of expensive/toxic reactants cannot yet be avoided.[30] Therefore, in the following, we assess $LiB_{11}H_{14}$:$LiCB_{11}H_{12}$ (1:1, Sample **H**) as a solid electrolyte (SE) for further electrochemical measurements and battery assembly.

In inorganic solid electrolytes, the ionic conductivity is predominately attributed to cation mobility and the anion mobility is negligible.[55] The electronic conductivity of Sample **E** was determined to be $\approx 5 \times 10^{-9}$ S cm^{-1} at 60 °C, by measuring the current decay in a Li/SE/Cu after applying constant voltages of 0.25 to 1 V (Figure S30, Supporting Information). The obtained electronic conductivity is one order of magnitude lower than 5×10^{-8} and 2.5×10^{-8} S cm^{-1} obtained at 60 °C for the typical solid electrolytes, $Li_7La_3Zr_2O_{12}$, and Li_3PS_4, respectively.[56]

2.5. Electrochemical Performance

To evaluate the stability of the $LiB_{11}H_{14}$:$LiCB_{11}H_{12}$ (1:1) SE against Li metal, a symmetric Li/SE/Li cell was assembled and the time evolution of the impedance spectra was measured at the open-circuit voltage. Impedance spectra were measured at intervals of 2 to 80 h, starting directly after contacting the Li metal with the SE to evaluate the interphase formation rate and its impact on the cell resistance over time. As depicted in **Figure 6**a, the evolution of the impedance was extracted using an equivalent circuit consisting of a constant phase element and two resistors representing the bulk and interphase resistances. Figure 6a also shows the Nyquist plots recorded at t = 6, 20, 40, 60, and 80 h. The extracted bulk and interphase resistances are presented in Figure 6b,c. Similar to sulfide-based solid electrolytes such as $Li_{10}GeP_2S_{12}$ and Li_3PS_4, our SE is not stable against Li metal and slowly decomposes over time.[57] The growth rate of the interphase obeys a parabolic rate law with a rate constant of k = 14.6 Ωcm^2 h$^{-0.5}$ obtained from the slope in Figure 6c, which is lower than the 45.1 and 1394.3 Ωcm^2 h$^{-0.5}$ reported for $Li_{10}GeP_2S_{12}$ and Li_6PS_5I, respectively.[58] However, this value is slightly higher than 2.9 and 3.8 Ωcm^2 h$^{-0.5}$ published for $Li_7P_3S_{11}$ and Li_6PS_5Cl, respectively.[58] The initial interphase resistance immediately after contacting the SE with Li metal is also calculated as 29.6 Ωcm^2 from the intercept in Figure 6c.

As previous studies have confirmed the stability of the $CB_{11}H_{12}^-$ anion against Li/Na metal,[18,19] we attribute the decomposition reaction on the anode side to the reduction of the $B_{11}H_{14}^-$ anion in the electrolyte. To get a better insight into possible decomposition reactions at the anode and cathode, we performed electrochemical stability calculations for $LiB_{11}H_{14}$[59,60] (for details of the present approach, see the DFT section in the Supporting Information and Figure S33 and Table S5, Supporting Information). DFT calculations show that $LiB_{11}H_{14}$ is unstable against Li metal, reducing to $Li_2B_{11}H_{13}$ (dashed rectangle in Figure 6f; and Table S5, Supporting Information). This reduction reaction requires the detachment of one proton and was also observed during the synthesis steps and when $(CH_3)_3NHB_{11}H_{14}$ was reacted with an excess amount of BuLi as a Li source (Figure 1c).

Although $LiB_{11}H_{14}$ appears to be unstable against Li metal, the SE/Li interphase shows sufficient ionic conductivity to support reversible electrodeposition as shown by the galvanostatic cycling of a symmetric Li/SE/Li cell. The galvanostatic cycling experiment (Figure 6d) reveals the excellent stability of >620 h at a current density of 25 or 50 μA cm^{-2}, switching the current direction every 1 or 10 h (0.50 mA cm^{-2}). A moderate increase in the overpotential from 22.5 to 30 mV after 620 h might be attributed to continuous and slow electrolyte reduction at the Li/SE interphase due to cracking of the formed $Li_2B_{11}H_{13}$ layer during electrodeposition. The critical current density (CCD) at which dendrites start to propagate through the SE was measured by increasing the current density in each cycle in a Li/SE/Li cell while keeping the transferred capacity per half cycle constant at 0.2 mAh cm^{-2} (Figure S31, Supporting Information). Using this method, a CCD of 0.16 mA cm^{-2} at 60 °C is determined. Similar CCD values of 0.04–0.28 mA cm^{-2} have been recently reported for single-crystalline $Li_{6.4}Ga_{0.2}La_3Zr_2O_{12}$ at ambient temperature.[61] Higher critical currents beyond 1 mA cm^{-2} typically require interface engineering to lower the interfacial resistance and external pressure in the MPa range applied on the cell to counteract void formation at the interface between Li metal and the electrolyte.[62–64]

In the next step, we experimentally determined the oxidative stability of the SE following the methodology of Asakura

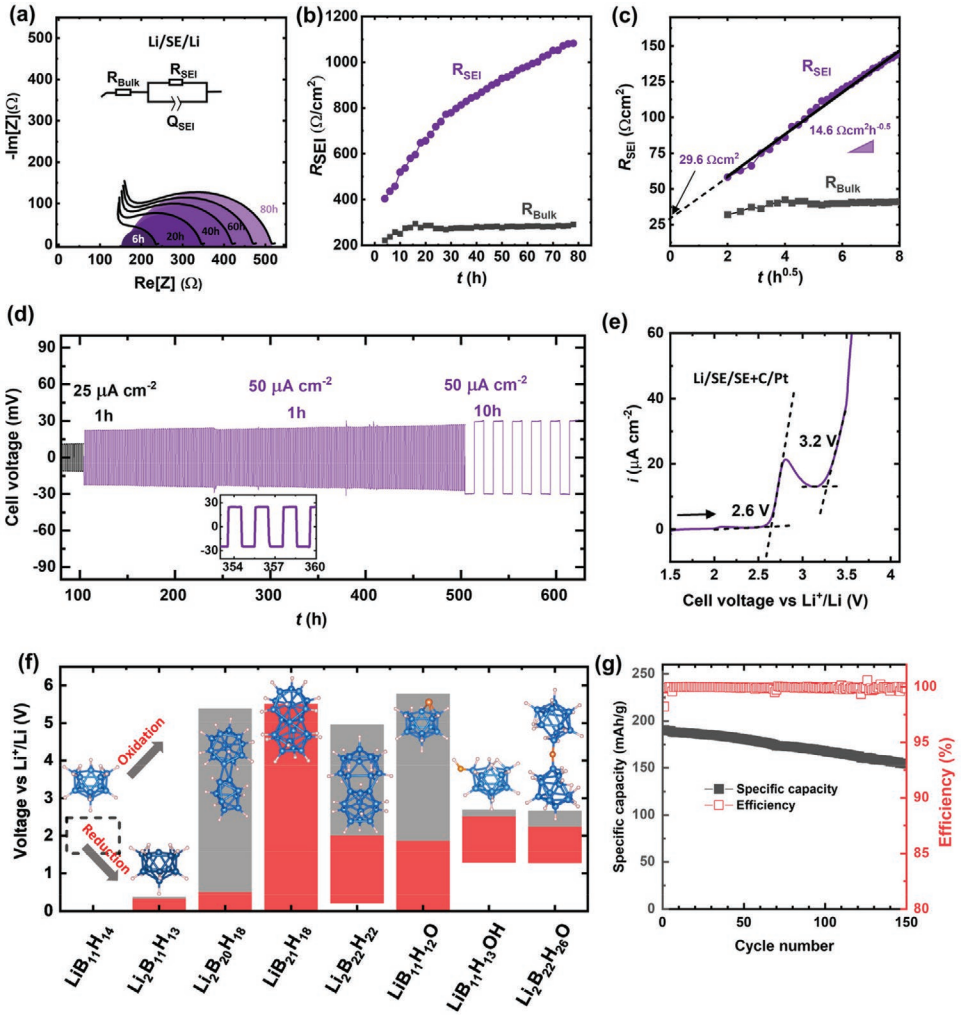

Figure 6. a) Nyquist plots and their equivalent circuit (fits) measured after 6–80 h of contacting the $LiB_{11}H_{14}$:$LiCB_{11}H_{12}$ (1:1) SE with Li metal. Solid electrolyte interface (SEI) and bulk resistances plotted versus b) time and c) square root of time to determine a parabolic rate constant. d) Galvanostatic cycling of a symmetric Li/SE/Li cell at current densities of 25 or 50 μA cm^{-2} (for 1 or 10 h in each direction). e) Voltammogram of a Li/SE/SE+C/Pt cell from 1.5 to 4.0 V versus Li$^+$/Li at a scan rate of 0.05 mV s^{-1}. f) Calculated electrochemical stability of selected hydroborate anions. $LiB_{11}H_{14}$ only appears as a stable compound in DFT calculations under specific assumptions (dashed rectangular, see Table S5, Supporting Information). The electrochemical stability of the other compounds was calculated with and without consideration of $LiB_{21}H_{18}$ as a final decomposition product in red and gray bars, respectively. g) Cycling performance and Coulombic efficiency of a Li/SE/TiS_2 cell cycled between 1.6 and 2.5 V versus Li$^+$/Li at C/10 (1st to 5th cycle) and C/5 (from 6th cyle) (1C = 0.239 mA g^{-1}) under 3.2 MPa. All measurements were performed at 60 °C.

et al. by linear sweep voltammetry.[65] The voltage of a SE/carbon composite working electrode was swept against a Li metal reference/counter electrode from 2.0 to 4.0 V versus Li$^+$/Li, as shown in Figure 6e. Similar to $NaB_{11}H_{14}$,[13] a clear onset of decomposition reactions is observed at ≈2.6 V versus Li$^+$/Li followed by a second onset at 3.2 V versus Li$^+$/Li. In the subsequent cycles, no significant current up to 4.0 V versus Li$^+$/Li is observed during both forward and backward scans (see Figure S32, Supporting Information), indicating the irreversibility of the decomposition products and the formation of a passivating, blocking layer during the first cycle.

DFT calculations were used to predict the electrochemical stability of the $LiB_{11}H_{14}$ together with other impurity compounds (**2**, **3**, **5**). It should be noted that the calculated electrochemical stability windows of the considered compounds depend on the selected decomposition products. Upon oxidation, electrolytes are typically delithiated. In this study, therefore, several poly-hydroborates with lower lithium content such as $LiB_{22}H_{22}$, $LiB_{21}H_{18}$, $LiB_{20}H_{18}$, and $B_{18}H_{22}$ are considered (see Table S5 and Figure S33 for the complete list, Supporting Information).[66] A $B_{22}H_{22}^{2-}$ compound was reported as the oxidation product of the $B_{11}H_{14}^-$ anion in solution[67] and trace amounts of $B_{21}H_{18}^-$ were observed in the MS data of Sample **B** (Table S2, Supporting Information). DFT calculations predict a narrow electrochemical window for $LiB_{11}H_{14}$ (dashed bar in Figure 6f) when only $B_{18}H_{22}$ as a completely delithiated and neutral borane is considered as the oxidation products (Figure S33 and Table S5, Supporting Information). The calculated stability window of $LiB_{11}H_{14}$ is comparable to Li_3PS_4[68] and is still larger than the calculated values for $Li_{10}GeP_2S_{12}$.[59,69] The list of the

electrochemical stability window of the most common solid electrolytes and their phase equilibria at their stability limits are presented in Table S6 (Supporting Information).

The electrochemical stability windows of the rest of the compounds were calculated with and without considering $LiB_{21}H_{18}$ as a decomposition product (red and gray bars in Figure 6f). DFT calculations suggest $LiB_{21}H_{18}$ as the most thermodynamically stable compound among the hydroborates considered here and can be perceived as the thermodynamic sink. It means that this compound tends to form as the oxidation product and is stable up to ≈5 V versus Li^+/Li before completely delithiating to $B_{18}H_{22}$ (red bars in Figure 6f).

A second series of calculations was carried out without considering the $LiB_{21}H_{18}$ as the decomposition product in order to stimulate that the formation of this compound is kinetically hindered. Under these assumptions, $Li_2B_{20}H_{18}$ and $Li_2B_{22}H_{22}$ are formed as the oxidation products and are stable up to ≈5 V versus Li^+/Li (gray bars).

In general, the $B_{11}H_{14}^-$ cage is prone to be oxidized by losing protons at the open side of the cage and subsequently forming poly-hydroborates. The same reaction is observed in aqueous media by replacing protons at the open side of the cage with an oxygen (compound **5**) or a hydroxyl group (compound **2**). Calculated electrochemical stability of these compounds (**2**, **3**, **5**) implies a wider electrochemical stability window compared to $LiB_{11}H_{14}$ (Figure 6f) and points toward a new strategy to synthesize them as a pure phase for the next generation of solid electrolytes.

The electronic conductivity of the decomposition products could be estimated by the following measurement. The Li/SE/Cu cell assembled for the electronic conductivity measurement shows an open-circuit voltage of ≈2.3 V. To measure the current response versus applied potential, constant voltages of 0.25, 0.5, 0.75, and 1 V were applied to the cell. When a constant voltage of ≥0.5 V is applied, the cell potential increases to >2.6 V versus Li^+/Li, which is above the electrochemical stability, and the SE starts to decompose. In these cases, smaller current responses are observed, suggesting the lower electronic conductivities of the decomposition products as a preferred requirement for the formation of a stable interphase (Figure S30b, Supporting Information).

Finally, a proof-of-concept battery using a Li metal anode and TiS_2 cathode was assembled in a home-built pressure cell. TiS_2 was selected as a cathode active material because of its lithium intercalation potential of ≤2.5 V versus Li^+/Li matches the oxidative stability limit of the SE. The chemical compatibility between the SE and the active material was further confirmed with PXRD. Figure S34 (Supporting Information) compares the PXRD patterns of the TiS_2, SE, and the SE/TiS_2 composite mixture annealed at 60 °C for 12 h (under vacuum, $p = 10^{-3}$ mbar). Unlike $LiBH_4$ that is unstable against TiS_2, leading to spontaneous lithiation upon heating with a shift of the PXRD patterns to lower 2θ angles,[70] no apparent reaction is observed between the SE and TiS_2 by PXRD. No shift of the PXRD patterns and formation of crystalline decomposition products are detected. Galvanostatic cycling of the cell at C/10 and C/5 (1C = 239 mA g^{-1}) under 3.2 MPa in Figure 6g shows a reversible discharge capacity of 190 mAh g^{-1} in the first cycle, corresponding to a TiS_2 utilization ratio of 80% compared to the theoretical capacity of 239 mAh g^{-1}.[71] Charge/discharge voltage profiles are presented in Figure S35 (Supporting Information). The Coulombic efficiency is as high as 98% in the first cycle, which stays at >99.5% in the later cycles. Switching C-rates to C/5 in the sixth cycle exhibits a minor decrease in discharge capacity (188 mAh g^{-1}). The reversible discharge capacity at C/5 retained 82% after 150 cycles (from 6th cycle), indicating stable battery cycling with a negligible oxidative decomposition of the SE. The slow cell degradation over cycling is attributed to the contact loss between the SE and the cathode active material together with the slow reductive decomposition of the electrolyte by the Li metal anode.

Improvements in battery performance, as well as the use of high voltage cathodes, could be made by using coated cathodes. This is a common approach for using sulfide-based solid electrolytes beyond their stability window and in combination with high-voltage cathodes. Summary lists of the electrochemical stability window of the most common solid electrolytes and their performances in all-solid-state lithium batteries are presented in Tables S6 and S7 (Supporting Information).[68,72]

3. Conclusion

In this work, we present for the first time, the synthesis of anhydrous $LiB_{11}H_{14}$ as a cost-effective building block for mixed-anion hydroborate lithium solid electrolytes. The impurity side products such as $LiB_{11}H_{13}OH$, $Li_2(B_{11}H_{13}\text{-}O\text{-}B_{11}H_{13})$, $Li(B_{11}H_{13}\text{-}O\text{-}Bu)$, and $LiB_{11}H_{12}O$ were thoroughly characterized by MS and NMR, and high purity $LiB_{11}H_{14}$ was obtained by excess use of Li source in the synthesis.

Disordered structures were obtained by partially replacing $LiB_{11}H_{14}$ with carba-*closo*-hydroborates. Ionic conductivity of 1.1×10^{-4} S cm^{-1} at 25 °C is achieved for $Li_2(B_{11}H_{14})(CB_{11}H_{12})$ and liquid-like ionic conductivity of up to 1.1×10^{-3} S cm^{-1} at 25 °C is achieved in a mixture with slightly smaller $LiCB_9H_{10}$ in the $Li_3(B_{11}H_{14})(CB_9H_{10})_2$. Therefore, contrary to the common trend that focuses on increasing the anion size and widening the ion conduction path, we propose focusing on small hydroborate anions which are more compatible with the small size of the Li^+ cation and enable suitable conduction channels.

$LiB_{11}H_{14}$ is not stable against Li metal; however, the formation of the Li-rich $Li_2B_{11}H_{13}$ allows electrodeposition in a symmetric cell with Li metal electrodes at 50 μA cm^{-2} (up to 0.5 mAh cm^{-2}) with a low overpotential increase which is stable over >620 cycles. The oxidative stability of 2.6 V versus Li^+/Li is obtained for this electrolyte is similar to Li_3PS_4 [68] but is narrower than that for *closo*-hydroborates due to the delocalized hydrogen atoms.[16,17]

In order to achieve high gravimetric energy densities, cathode materials such as $Li_2C_6O_6$[73] or sulfur [18] with a theoretical capacity of 590 and 1675 mAh g^{-1}, respectively, are suggested, which lie within the stability window. In this regard, we assembled a proof-of-concept battery using TiS_2 cathode which matches the oxidative stability of the electrolyte. The other common strategy is to use protective coatings together with high-voltage cathodes as a common method for sulfide-based ASSBs.[68,72] Finally, the intrinsic stability of the electrolyte could be improved by replacing hydrogen atoms with an

O atom or an OH group as suggested by DFT calculations or closing the cage with Sn and P form $SnB_{11}H_{11}^{2-}$ and $PB_{11}H_{11}^{-}$ compounds.[74,75] Therefore, $LiB_{11}H_{14}$ as a cost-effective building block opens a new chapter for designing novel hydroborate-based solid electrolytes for all-solid-state lithium batteries.

[CCDC 2 043 896, 20 438 972 043 898, 2 043 899, 2 043 900 contain the supplementary crystallographic data for this paper. These data can be obtained free of charge from The Cambridge Crystallographic Data Centre via www.ccdc.cam.ac.uk/data_request/cif.]

Supporting Information

Supporting Information is available from the Wiley Online Library or from the author.

Acknowledgements

S.P. thanks Petroula Avramidou for the helpful discussions. The authors thank the Swiss National Science Foundation (SNSF) for financial support via Grant No. 200021L_192191. S.P. was supported by the EMPAPOSTDOCS-II program, which has received funding from the European Union's Horizon 2020 research and innovation program under the Marie Skłodowska-Curie Grant Agreement No. 754364. The NMR hardware was partially granted by the SNSF Grant No. 206021_150638/1. Z.L. acknowledges NCN support through 2019/01/Y/ST5/00046 Alphorn Project and CPU al-location at PL-Grid infrastructure.

Conflict of Interest

The authors declare no conflict of interest.

Data Availability Statement

Research data are not shared.

Keywords

electrolyte stability, hydroborate, $LiB_{11}H_{14}$, lithium tetradecahydroundecaborate, *nido*-hydroborate, solid-state batteries, solid-state electrolytes

Received: November 22, 2020
Revised: January 22, 2021
Published online:

[1] S. Randau, D. A. Weber, O. Kötz, R. Koerver, P. Braun, A. Weber, E. Ivers-Tiffée, T. Adermann, J. Kulisch, W. G. Zeier, F. H. Richter, J. Janek, *Nat. Energy* **2020**, *5*, 259.
[2] A. Manthiram, X. Yu, S. Wang, *Nat. Rev. Mater.* **2017**, *2*, 16103.
[3] V. Thangadurai, S. Narayanan, D. Pinzaru, *Chem. Soc. Rev.* **2014**, *43*, 4714.
[4] C. Wang, K. Fu, S. P. Kammampata, D. W. McOwen, A. J. Samson, L. Zhang, G. T. Hitz, A. M. Nolan, E. D. Wachsman, Y. Mo, V. Thangadurai, L. Hu, *Chem. Rev.* **2020**, *120*, 4257.
[5] Q. Zhang, D. Cao, Y. Ma, A. Natan, P. Aurora, H. Zhu, *Adv. Mater.* **2019**, *31*, 1901131.
[6] S. Wenzel, S. Randau, T. Leichtweiß, D. A. Weber, J. Sann, W. G. Zeier, J. Janek, *Chem. Mater.* **2016**, *28*, 2400.
[7] X. Li, J. Liang, X. Yang, K. R. Adair, C. Wang, F. Zhao, X. Sun, *Energy Environ. Sci.* **2020**, *13*, 1429.
[8] X. Li, J. Liang, N. Chen, J. Luo, K. R. Adair, C. Wang, M. N. Banis, T. K. Sham, L. Zhang, S. Zhao, S. Lu, H. Huang, R. Li, X. Sun, *Angew. Chem., Int. Ed.* **2019**, *58*, 16427.
[9] T. Asano, A. Sakai, S. Ouchi, M. Sakaida, A. Miyazaki, S. Hasegawa, *Adv. Mater.* **2018**, *30*, 1803075.
[10] P. Yao, H. Yu, Z. Ding, Y. Liu, J. Lu, M. Lavorgna, J. Wu, X. Liu, *Front. Chem.* **2019**, *7*, 522.
[11] B. R. S. Hansen, M. Paskevicius, H. W. Li, E. Akiba, T. R. Jensen, *Coord. Chem. Rev.* **2016**, *323*, 60.
[12] R. Mohtadi, S. Orimo, *Nat. Rev. Mater.* **2016**, *2*, 16091.
[13] S. Payandeh, R. Asakura, P. Avramidou, D. Rentsch, Z. Łodziana, R. Černý, A. Remhof, C. Battaglia, *Chem. Mater.* **2020**, *32*, 1101.
[14] W. S. Tang, M. Dimitrievska, V. Stavila, W. Zhou, H. Wu, A. A. Talin, T. J. Udovic, *Chem. Mater.* **2017**, *29*, 10496.
[15] W. S. Tang, K. Yoshida, A. V. Soloninin, R. V. Skoryunov, O. A. Babanova, A. V. Skripov, M. Dimitrievska, V. Stavila, S. I. Orimo, T. J. Udovic, *ACS Energy Lett.* **2016**, *1*, 659.
[16] L. Duchêne, R.-S. Kühnel, D. Rentsch, A. Remhof, H. Hagemann, C. Battaglia, *Chem. Commun.* **2017**, *53*, 4195.
[17] M. Brighi, F. Murgia, Z. Łodziana, P. Schouwink, A. Wolczyk, R. Černý, *J. Power Sources* **2018**, *404*, 7.
[18] S. Kim, H. Oguchi, N. Toyama, T. Sato, S. Takagi, T. Otomo, D. Arunkumar, N. Kuwata, J. Kawamura, S. Orimo, *Nat. Commun.* **2019**, *10*, 1081.
[19] F. Murgia, M. Brighi, R. Černý, *Electrochem. Commun.* **2019**, *106*, 106534.
[20] E. Hadjixenophontos, E. M. Dematteis, N. Berti, A. R. Wołczyk, P. Huen, M. Brighi, T. T. Le, A. Santoru, S. Payandeh, F. Peru, A. H. Dao, Y. Liu, M. Heere, *Inorganics* **2020**, *8*, 17.
[21] L. Duchêne, A. Remhof, H. Hagemann, C. Battaglia, *Energy Storage Mater.* **2020**, *25*, 782.
[22] J. Cuan, Y. Zhou, T. Zhou, S. Ling, K. Rui, Z. Guo, H. Liu, X. Yu, *Adv. Mater.* **2019**, *31*, 1803533.
[23] M. Brighi, F. Murgia, R. Černý, *Cell Reports Phys. Sci.* **2020**, *1*, 100217.
[24] R. Moury, Z. Łodziana, A. Remhof, L. Duchêne, E. Roedern, A. Gigante, H. Hagemann, *Acta Crystallogr., Sect. B: Struct. Sci., Cryst. Eng. Mater.* **2019**, *75*, 406.
[25] W. S. Tang, M. Matsuo, H. Wu, V. Stavila, W. Zhou, A. A. Talin, A. V. Soloninin, R. V. Skoryunov, O. A. Babanova, A. V. Skripov, A. Unemoto, S.-I. Orimo, T. J. Udovic, *Adv. Energy Mater.* **2016**, *6*, 1502237.
[26] M. Jørgensen, P. T. Shea, A. W. Tomich, J. B. Varley, M. Bercx, S. Lovera, R. Černý, W. Zhou, T. J. Udovic, V. Lavallo, T. R. Jensen, B. C. Wood, V. Stavila, *Chem. Mater.* **2020**, *32*, 1475.
[27] L. Duchêne, D. H. Kim, Y. B. Song, S. Jun, R. Moury, A. Remhof, H. Hagemann, Y. S. Jung, C. Battaglia, *Energy Storage Mater.* **2020**, *26*, 543.
[28] R. Asakura, D. Reber, L. Duchêne, S. Payandeh, A. Remhof, H. Hagemann, C. Battaglia, *Energy Environ. Sci.* **2020**, *13*, 5048.
[29] S. Kim, K. Kisu, S. Takagi, H. Oguchi, S. I. Orimo, *ACS Appl. Energy Mater.* **2020**, *3*, 4831.
[30] B. Ringstrand, D. Bateman, R. K. Shoemaker, Z. Janoušek, *Collect. Czech. Chem. Commun.* **2009**, *74*, 419.
[31] G. B. Dunks, K. Barker, E. Hedaya, C. Hefner, K. Palmer-Ordonez, P. Remec, *Inorg. Chem.* **1981**, *20*, 1692.
[32] S. Pylypko, S. Ould-Amara, A. Zadick, E. Petit, M. Chatenet, M. Cretin, U. B. Demirci, *Appl. Catal., B* **2018**, *222*, 1.
[33] M. Paskevicius, B. R. S. Hansen, M. Jørgensen, B. Richter, T. R. Jensen, *Nat. Commun.* **2017**, *8*, 15136.
[34] A. Ouassas, B. Fenet, H. Mongeot, B. Gautheron, E. Barday, B. Frange, *J. Chem. Soc., Chem. Commun.* **1995**, *1*, 1663.

[35] A. Ouassas, C. R'Kha, H. Mongeot, B. Frange, *Inorg. Chim. Acta* **1991**, *180*, 257.
[36] S. Hermanek, *Chem. Rev.* **1992**, *92*, 325.
[37] C. E. C. A. Hop, D. A. Saulys, D. F. Gaines, *Inorg. Chem.* **1995**, *34*, 1977.
[38] J. D. Kennedy, N. N. Greenwood, *Inorg. Chim. Acta* **1980**, *38*, 93.
[39] J. H. Her, M. Yousufuddin, W. Zhou, S. S. Jalisatgi, J. G. Kulleck, J. A. Zan, S. J. Hwang, R. C. Bowman, T. J. Udovic, *Inorg. Chem.* **2008**, *47*, 9757.
[40] H. Wu, W. S. Tang, V. Stavila, W. Zhou, J. J. Rush, T. J. Udovic, *J. Phys. Chem. C* **2015**, *119*, 6481.
[41] L. Pauling, *J. Am. Chem. Soc.* **1929**, *51*, 1010.
[42] R. Černý, M. Brighi, F. Murgia, *Chemistry* **2020**, *2*, 805.
[43] R. D. Shannon, *Acta Crystallogr., Sect. A: Found. Crystallogr.* **1976**, *32*, 751.
[44] W. S. Tang, A. Unemoto, W. Zhou, V. Stavila, M. Matsuo, H. Wu, S. Orimo, T. J. Udovic, *Energy Environ. Sci.* **2015**, *8*, 3637.
[45] Y. Sadikin, *Ph.D. Thesis*, Geneva University, **2016**.
[46] Y. Wang, W. D. Richards, S. P. Ong, L. J. Miara, J. C. Kim, Y. Mo, G. Ceder, *Nat. Mater.* **2015**, *14*, 1026.
[47] L. Duchêne, S. Lunghammer, T. Burankova, W. C. Liao, J. P. Embs, C. Copéret, H. M. R. Wilkening, A. Remhof, H. Hagemann, C. Battaglia, *Chem. Mater.* **2019**, *31*, 3449.
[48] F. A. Kiani, M. Hofmann, *Inorg. Chem.* **2006**, *45*, 6996.
[49] E. Bernhardt, D. J. Brauer, M. Finze, H. Willner, *Angew. Chem., Int. Ed.* **2007**, *46*, 2927.
[50] M. Paskevicius, M. P. Pitt, D. H. Brown, D. A. Sheppard, S. Chumphongphan, C. E. Buckley, *Phys. Chem. Chem. Phys.* **2013**, *15*, 15825.
[51] A. Gigante, L. Duchêne, R. Moury, M. Pupier, A. Remhof, H. Hagemann, *ChemSusChem* **2019**, *4*, 4832.
[52] Y. Yan, D. Rentsch, C. Battaglia, A. Remhof, *Dalt. Trans.* **2017**, *46*, 12434.
[53] A. Unemoto, K. Yoshida, T. Ikeshoji, S. I. Orimo, *Mater. Trans.* **2016**, *57*, 1639.
[54] L. Duchêne, S. Lunghammer, T. Burankova, W.-C. Liao, J. P. Embs, C. Copéret, H. M. R. Wilkening, A. Remhof, H. Hagemann, C. Battaglia, *Chem. Mater.* **2019**, *31*, 3449.
[55] P. Kurzweil, K. Brandt, *Electrochemical Power Sources: Fundamentals, Systems, and Applications* (Eds: J. Garche, K. Brandt), Elsevier, Amsterdam **2019**, pp. 47–82.
[56] F. Han, A. S. Westover, J. Yue, X. Fan, F. Wang, M. Chi, D. N. Leonard, N. J. Dudney, H. Wang, C. Wang, *Nat. Energy* **2019**, *4*, 187.
[57] Y. Zhu, X. He, Y. Mo, *ACS Appl. Mater. Interfaces* **2015**, *7*, 23685.
[58] S. Wenzel, S. J. Sedlmaier, C. Dietrich, W. G. Zeier, J. Janek, *Solid State Ionics* **2018**, *318*, 102.
[59] W. D. Richards, L. J. Miara, Y. Wang, J. C. Kim, G. Ceder, *Chem. Mater.* **2016**, *28*, 266.
[60] A. E. Maniadaki, Z. Łodziana, *Phys. Chem. Chem. Phys.* **2018**, *20*, 30140.
[61] F. Flatscher, M. Philipp, S. Ganschow, H. M. R. Wilkening, D. Rettenwander, *J. Mater. Chem. A* **2020**, *8*, 15782.
[62] M. C. Bay, M. Wang, R. Grissa, M. V. F. Heinz, J. Sakamoto, C. Battaglia, *Adv. Energy Mater.* **2020**, *10*, 1902899.
[63] J. Kasemchainan, S. Zekoll, D. S. Jolly, Z. Ning, G. O. Hartley, J. Marrow, P. G. Bruce, *Nat. Mater.* **2019**, *18*, 1105.
[64] M. Wang, J. B. Wolfenstine, J. Sakamoto, *Electrochim. Acta* **2019**, *296*, 842.
[65] R. Asakura, L. Duchêne, R.-S. Kühnel, A. Remhof, H. Hagemann, C. Battaglia, *ACS Appl. Energy Mater.* **2019**, *2*, 6924.
[66] O. Shameema, E. D. Jemmis, *Chem. - Asian J.* **2009**, *4*, 1346.
[67] N. S. Hosmane, A. Franken, G. Zhang, R. R. Srivastava, R. Y. Smith, B. F. Spielvogel, *MainGr. Met. Chem.* **1998**, *21*, 319.
[68] Y. Xiao, L. J. Miara, Y. Wang, G. Ceder, *Joule* **2019**, *3*, 1252.
[69] Y. Mo, S. P. Ong, G. Ceder, *Chem. Mater.* **2012**, *24*, 15.
[70] A. Unemoto, T. Ikeshoji, S. Yasaku, M. Matsuo, V. Stavila, J. Terrence, *Chem. Mater* **2015**, *27*, 5407.
[71] M. S. Whittingham, *Science* **1976**, *192*, 1126 LP.
[72] A. Y. Kim, F. Strauss, T. Bartsch, J. H. Teo, T. Hatsukade, A. Mazilkin, J. Janek, P. Hartmann, T. Brezesinski, *Chem. Mater.* **2019**, *31*, 9664.
[73] C. Lu, C. Dong, H. Wu, D. Ni, W. Sun, Z. Wang, K. Sun, *Chem. Commun.* **2018**, *54*, 3235.
[74] R. W. Chapman, J. G. Kester, K. Folting, W. E. Streib, L. J. Todd, *Inorg. Chem.* **1992**, *31*, 979.
[75] J. L. Little, M. A. Whitesell, R. W. Chapman, J. G. Kester, J. C. Huffman, L. J. Todd, *Inorg. Chem.* **1993**, *32*, 3369.